Journal of The Korean Astronomical Society
**45**: 127 ∼ 138, 2012 October

http://dx.doi.org/10.5303/JKAS.2012.45.5.127
ISSN:1225-4614
http://jkas.kas.org

# DIFFUSIVE SHOCK ACCELERATION WITH MAGNETIC FIELD AMPLIFICATION AND ALFVÉNIC DRIFT

Hyesung Kang
Department of Earth Sciences, Pusan National University, Pusan 609-735, Korea
*E-mail : hskang@pusan.ac.kr*
*(Received August 3, 2012; Revised September 12, 2012; Accepted September 13, 2012)*

## ABSTRACT

We explore how wave-particle interactions affect diffusive shock acceleration (DSA) at astrophysical shocks by performing time-dependent kinetic simulations, in which phenomenological models for magnetic field amplification (MFA), Alfvénic drift, thermal leakage injection, Bohm-like diffusion, and a free escape boundary are implemented. If the injection fraction of cosmic-ray (CR) particles is $\xi > 2\times 10^{-4}$, for the shock parameters relevant for young supernova remnants, DSA is efficient enough to develop a significant shock precursor due to CR feedback, and magnetic field can be amplified up to a factor of 20 via CR streaming instability in the upstream region. If scattering centers drift with Alfvén speed in the amplified magnetic field, the CR energy spectrum can be steepened significantly and the acceleration efficiency is reduced. Nonlinear DSA with self-consistent MFA and Alfvénic drift predicts that the postshock CR pressure saturates roughly at $\sim 10$ % of the shock ram pressure for strong shocks with a sonic Mach number ranging $20 \lesssim M_s \lesssim 100$. Since the amplified magnetic field follows the flow modification in the precursor, the low energy end of the particle spectrum is softened much more than the high energy end. As a result, the concave curvature in the energy spectra does not disappear entirely even with the help of Alfvénic drift. For shocks with a moderate Alfvén Mach number ($M_A < 10$), the accelerated CR spectrum can become as steep as $E^{-2.1} - E^{-2.3}$, which is more consistent with the observed CR spectrum and gamma-ray photon spectrum of several young supernova remnants.

*Key words :* cosmic ray acceleration — shock wave — hydrodynamics — methods: numerical

## 1. INTRODUCTION

Diffusive shock acceleration (DSA) theory explains how nonthermal particles are produced through their interactions with MHD waves in the converging flows across collisionless shocks in astrophysical plasmas (Bell 1978; Drury 1983; Blandford & Eichler 1987). Theoretical studies have shown that some suprathermal particles with velocities large enough to swim against the downstream flow can return across the shock and stream upstream, and that streaming motions of high energy particles against the background fluid generate both resonant and nonresonant waves upstream of the shock (Bell 1978; Lucek & Bell 2000; Bell 2004; Riquelme & Spitkovsky 2009; Rogachevskii et al. 2012). Those waves in turn scatter CR particles and amplify turbulent magnetic fields in the preshock region. These plasma physical processes, i.e., injection of suprathermal particles into the CR population, self-excitation of MHD waves, and amplification of magnetic fields are all integral parts of DSA (e.g., Malkov & Drury 2001).

Multi-band observations of nonthermal radio to $\gamma$-ray emissions from supernova remnant (SNR) shocks have confirmed the acceleration of CR electrons and protons up to $\sim 100$ TeV (e.g., Abdo et al. 2010, 2011; Acero et al. 2010; Acciari et al. 2011; Giordano et al. 2012). Moreover, thin rims of several young SNRs in high-resolution X-ray observations indicate the presence of downstream magnetic fields as strong as a few $100\mu$G, implying efficient magnetic field amplification (MFA) at these shocks (e.g., Parizot et al. 2006; Eriksen et al. 2011; Reynolds et al. 2012).

The most attractive feature of the DSA theory is the simple prediction of power-law energy spectra of CRs, $N(E) \propto E^{-(\sigma+2)/(\sigma-1)}$ (where $\sigma$ is the shock compression ratio) in the test particle limit. For strong, adiabatic gas shocks with $\sigma = 4$, this gives a power-law index of 2, which is reasonably close to the observed 'universal' index of the CR spectra in many environments. However, nonlinear treatments of DSA predict that at strong shocks there are highly nonlinear back-reactions from CRs to the underlying flow, creating a shock precursor (e.g., Berezhko & Völk 1997; Kang & Jones 2007). So the particles just above the injection momentum ($p_{\rm inj}$) sample mostly the compression across the subshock ($\sigma_s$), while those near the highest momentum ($p_{\rm max}$) experience the greater, total compression across the entire shock structure ($\sigma_t$). This leads to the CR energy spectrum that behaves as $N(E) \propto E^{-(\sigma_s+2)/(\sigma_s-1)}$ for $p \sim p_{\rm inj}$, but flattens gradually to $N(E) \propto E^{-(\sigma_t+2)/(\sigma_t-1)}$ toward $p \sim p_{\rm max}$ (Kang et al. 2009). For example, the power-law index

becomes 1.5 for $\sigma_t = 7$.

In contrast to such expectations, however, the GeV-TeV $\gamma$-ray spectra of several young SNRs seem to require the proton spectrum as steep as $N(E) \propto E^{-2.3}$, if the observed $\gamma$-ray photons indeed originate from $\pi^0$ decay (Abdo et al. 2010; Giordano et al. 2012). This is even softer than the test-particle power-law for strong shocks. Moreover, Ave et al. (2009) showed that the spectrum of CR nuclei observed at Earth can be fitted by a single power law of $J(E) \propto E^{-2.67}$ below $10^{14}$ eV. Assuming an energy-dependent propagation path length ($\Lambda \propto E^{-0.6}$), they suggested that a soft source spectrum, $N(E) \propto E^{-\alpha}$ with $\alpha \sim 2.3 - 2.4$ is preferred by the observed data. These observational data appear to be inconsistent with flat CR spectra predicted by nonlinear DSA model for the SNR origin of Galactic CRs.

It has been suggested that non-linear wave damping and wave dissipation due to ion-neutral collisions may weaken the stochastic scattering on relevant scales, leading to slower acceleration than predicted based on the the so-called Bohm-like diffusion, and escape of the highest energy particles from the shock (e.g., Ptuskin & Zirakashvili 2005; Caprioli et al. 2009). These processes may lead to the particle energy spectrum at the highest energy end that is much steeper than predicted by nonlinear DSA. Escape of high energy protons from SNRs is an important and very complex problem that needs further investigation (Malkov et al. 2011; Drury 2011).

Recently some serious efforts have been undertaken to understand at least some of the complex plasma processes through Particle-in-Cell (PIC) and hybrid plasma simulations (e.g., Riquelme & Spitkovsky 2009; Guo et al. 2012; Garaté & Spitkovsky 2012). However, these types of plasma simulations are too demanding and expensive to be able to study the full extent of the DSA problem. So we do not yet understand them in enough detail to make precise quantitative predictions for the injection and acceleration rate and efficiency. Instead, most kinetic approaches commonly adopt phenomenological models that can emulate more or less self-consistently some of those plasma interactions, for example, the thermal leakage injection, magnetic field amplification, wave-damping, etc. (e.g., Berezhko et al. 2009; Kang 2010; Ptuskin et al. 2010; Lee et al. 2012; Caprioli 2012).

In our previous studies, we considered DSA of CR protons, assuming that magnetic field strength is uniform in space and constant in time without self-consistent MFA (e.g., Kang & Jones 2007; Kang et al. 2009). In the present paper, we explore how the following processes affect the energy spectra of CR protons and electrons accelerated at plane astrophysical shocks: 1) magnetic field amplified by CR streaming instability in the precursor 2) drift of scattering centers with Alfvén speed in the *amplified magnetic field*, and 3) escape of highest energy particles from the shock. Toward this end we have performed time-dependent numerical simulations, in which DSA of CR protons and electrons at strong planar shocks is followed along with electronic synchrotron and inverse Compton (IC) losses. Magnetic field amplification due to resonant waves generated by CR streaming instability is included through an approximate, analytic model suggested by Caprioli (2012). Escape of the highest energy particles near the maximum momentum, $p_{\rm max}$, is included by implementing a free escape boundary (FEB) at an upstream location. As in our previous works (e.g., Kang 2010, 2011), a thermal leakage injection model, a Bohm-like diffusion coefficient ($\kappa(p) \propto p$), and a model for wave dissipation and heating of the gas are adopted as well.

In the next section we describe the numerical method and phenomenological models for the plasma interactions in DSA theory, and the model parameters for planar shocks. The simulation results will be discussed in Section 3, followed by a brief summary in Section 4.

## 2. DSA MODEL

### 2.1 CRASH Code for DSA

Here we consider the CR acceleration at quasi-parallel shocks where the mean background magnetic field lines are parallel to the shock normal. So we solve the standard gasdynamic equations with CR proton pressure terms added in the conservative, Eulerian formulation for one dimensional plane-parallel geometry. The basic gasdynamic equations and details of the CRASH (Cosmic-Ray Amr SHock) code can be found in Kang et al. (2002) and Kang (2011).

We solve the following diffusion-convection equations for the pitch-angle-averaged phase space distribution function for CR protons, $g_p = f_p p^4$, and for CR electron, $g_e = f_e p^4$ (Skilling 1975):

$$\frac{\partial g}{\partial t} + (u+u_w)\frac{\partial g}{\partial x} = \frac{1}{3}\frac{\partial}{\partial x}(u+u_w)\left(\frac{\partial g}{\partial y} - 4g\right) + \frac{\partial}{\partial x}\left[\kappa(x,y)\frac{\partial g}{\partial x}\right] + p\frac{\partial}{\partial y}\left(\frac{b}{p^2}g\right), \quad (1)$$

where $y = \ln(p/m_p c)$. Here the particle momentum is expressed in units of $m_p c$ and so the spatial diffusion coefficient, $\kappa(x,p)$, has the same form for *both protons and electrons*. The velocity $u_w$ represents the effective relative motion of scattering centers with respect to the bulk flow velocity, $u$, which will be described in detail in Section 2.5.

The cooling term $b(p) = -dp/dt$ accounts for electron synchrotron/IC losses, while it is set to be $b(p) = 0$ for protons. The synchrotron/IC cooling constant for electrons is defined as

$$b(p) = \frac{4e^4}{9m_e^4 c^6} B_{\rm e}^2 p^2 \quad (2)$$

in cgs units, where $e$ and $m_e$ are electron charge and mass, respectively. Here $B_e^2 = B^2 + B_r^2$ as the effective magnetic field strength for radiative losses including the energy density of the ambient radiation field. We set $B_r = 6.5\ \mu$G, including the cosmic background and mean Galactic radiation fields (Edmon et al. 2011).

The dynamical effects of the CR proton pressure are included in the DSA simulations, while the CR electrons are treated as test-particles. In order to include the dynamical effects of amplified magnetic field, the magnetic pressure, $P_B = B^2/8\pi$, is added to the momentum conservation equation as follows:

$$\frac{\partial(\rho u)}{\partial t} + \frac{\partial(\rho u^2 + P_g + P_c + P_B)}{\partial x} = 0. \quad (3)$$

However, our model magnetic field amplification typically results in $P_B/\rho_0 u_s^2 < 0.01$ in the precursor, where $\rho_0 u_s^2$ is the shock ram pressure (see Section 2.4).

### 2.2 Thermal Leakage Injection

The injection rate with which suprathermal particles are injected into CRs at the subshock depends in general upon the shock Mach number, field obliquity angle, and strength of Alfvénic turbulence responsible for scattering. In thermal leakage injection models suprathermal particles well into the exponential tail of the postshock Maxwellian distribution leak upstream across a quasi-parallel shock (Malkov & Drury 2001; Kang et al. 2002). We adopt a simple injection scheme in which the particles above an effective injection momentum $p_{\rm inj}$ cross the shock and get injected to the CR population:

$$p_{\rm inj} \approx 1.17 m_p u_2 \left(1 + \frac{1.07}{\epsilon_B}\right), \quad (4)$$

where the injection parameter, $\epsilon_B = B_0/B_\perp$, is the ratio of the large-scale magnetic field along the shock normal, $B_0$, to the amplitude of the postshock MHD wave turbulence, $B_\perp$ (Kang et al. 2002). With a larger value of $\epsilon_B$ (i.e., weaker turbulence), $p_{\rm inj}$ is smaller, which results in a higher injection rate. We consider $\epsilon_B = 0.23$ here.

We define the injection efficiency as the fraction of particles that have entered the shock from far upstream and then injected into the CR distribution:

$$\xi(t) = \frac{\int dx \int_{p_{\rm inj}}^{\infty} 4\pi f_p(p,x,t) p^2 dp}{n_0 u_s t}, \quad (5)$$

where $n_0$ is the particle number density far upstream and $u_s$ is the shock speed.

Since postshock thermal electrons need to be preaccelerated before they can be injected into Fermi process, it is expected that electrons are injected at the shock with a much smaller injection rate, i.e., the CR electron-to-proton ratio is estimated to be small, $K_{e/p} \sim 10^{-4} - 10^{-2}$ (Reynolds 2008; Morlino & Caprioli 2012). Since this ratio is not yet constrained accurately by plasma physics and we do not consider nonthermal emissions from CR particles in this paper, both protons and electrons are injected in the same manner in our simulations (i.e., we use $K_{e/p} = 1$). But $K_{e/p} = 0.1$ will be used just for clarity for some figures below.

### 2.3 Bohm-Like Diffusion Model

It is assumed that CR particles are resonantly scattered by Alfvén waves, which are excited by CR streaming instability in the upstream region and then advected and compressed in the down stream region (Bell 1978; Lucek & Bell 2000). So in DSA modeling the Bohm diffusion model, $\kappa_B = (1/3) r_g v$, is commonly used to represent a saturated wave spectrum. We adopt a Bohm-like diffusion coefficient that includes a flattened non-relativistic momentum dependence,

$$\kappa(x,p) = \kappa_{\rm n} \frac{B_0}{B_\parallel(x)} \cdot \frac{p}{m_p c}, \quad (6)$$

where $\kappa_n = m_p c^3/(3eB_0) = (3.13 \times 10^{22} {\rm cm^2 s^{-1}}) B_0^{-1}$, and $B_0$ is the magnetic field strength far upstream expressed in units of microgauss. The parallel component of the local magnetic field strength, $B_\parallel(x)$, will be described in the next section. Hereafter we use the subscripts '0', '1', and '2' to denote conditions far upstream of the shock, immediately upstream and downstream of the subshock, respectively.

### 2.4 Magnetic Field Amplification

Since the resonant interactions amplify mainly the turbulent magnetic field perpendicular to the shock normal in the quasi-linear limit, it was commonly assumed that the parallel component is the unperturbed upstream field, $B_\parallel \approx B_0$ (Caprioli et al. 2009). In the case of a strong MFA, however, the wave-particle interaction and the CR transport are not yet understood fully. For example, plasma simulations by Riquelme & Spitkovsky (2009) showed that both $B_\parallel/B_0$ and $B_\perp/B_0$ can increase to $\sim 10 - 30$ via Bell's CR current driven instability. Here we follow the prescription for MFA that was formulated by Caprioli (2012) based on the assumption of isotropization of amplified magnetic field.

In the upstream region ($x > x_s$),

$$\frac{B(x)^2}{B_0^2} = 1 + (1 - \omega_H) \cdot \frac{4}{25} M_{A,0}^2 \frac{(1 - U(x)^{5/4})^2}{U(x)^{3/2}}, \quad (7)$$

where $B^2 = B_\parallel^2 + B_\perp^2$, $M_{A,0} = u_s/v_{A,0}$ is the Alfvén Mach number for the far upstream Alfvén speed, $v_{A,0} = B_0/\sqrt{4\pi\rho_0}$, and $U(x) = [u_s - u(x)]/u_s$ is the flow speed in the shock rest frame normalized by the shock speed. The factor $(1-\omega_H)$ is introduced to take account of the loss of magnetic energy due to wave dissipation, which

will be discussed in Section 2.5. Obviously, $\omega_H = 0$ means no dissipation, while $\omega_H = 1$ means complete dissipation of waves (i.e., no MFA). Here $\omega_H = 0.1$ will be considered as a fiducial case, since we are interested in the case where the effects of MFA and the ensuing wave drift are the greatest.

This MFA model predicts no amplification in the test-particle regime, where the flow structure is not modified (i.e., $U(x) = 1$). In the case of "moderately modified" shocks, for example, if $U_1 \approx 0.8$ and $\omega_H = 0.1$, the amplified magnetic field strength scales as $B_1/B_0 \approx 0.11 M_{A,0}$. So for $M_{A,0} \approx 150$, the preshock amplification factor could become $B_1/B_0 \approx 17$. On the other hand, the ratio of the magnetic pressure to the shock ram pressure becomes $P_{B,1}/\rho_0 u_s^2 = (2/25)(1-U_1^{5/4})^2/U_1^{3/2} \approx 6.6\times10^{-3}$. So we expect that even the amplified field is not dynamically important in the precursor.

The magnetic field strength immediately upstream of the subshock, $B_1$, is estimated by using Eq. 7 and assumed to be completely turbulent. Moreover, assuming that the two perpendicular components are simply compressed across the subshock, the immediate postshock field strength can be estimated by

$$B_2/B_1 = \sqrt{1/3 + 2/3(\rho_2/\rho_1)^2}. \tag{8}$$

So for the case with $\rho_2/\rho_1 \approx 4.2$, $B_2/B_1 \approx 3.5$. Then we assume that in the downstream region the field strength scales with the gas density:

$$B(x) = B_2 \cdot [\rho(x)/\rho_2]\,. \tag{9}$$

We note that the MFA model described in Eqs. 7-9 is also used for the diffusion coefficient model given by Eq. 6. Hence the maximum momentum $p_{\rm max}$ is controlled by the degree of MFA as well.

### 2.5 Alfvénic Drift

The resonant waves generated by CR streaming instability will drift with respect to the underlying flow and also transfer energy to the gas through dissipation (e.g., Skilling 1975; Jones 1993). These two effects influence the accelerated particle spectrum and the DSA efficiency as follows. The scattering by Alfvén waves tends to isotropize the CR distribution in the wave frame rather than in the gas frame (Bell 1978), which reduces the velocity difference between upstream and downstream scattering centers, compared to that of the bulk flow. The resulting CR spectrum becomes softer than estimated without considering the wave drift.

The mean drift speed of scattering centers is commonly set to be the Alfvén speed, i.e., $u_{w,1}(x) = +v_A$, pointing away from the shock. As described in Eq. 7, we assume that both $B_\parallel$ and $B_\perp$ are amplified and isotropized, and so scattering centers drift with Alfvén speed in the local amplified magnetic field. In order to account for the uncertainty regarding this issue, we model the local Aflvén speed as

$$v_A(x) = \frac{B_0 + (B_\parallel(x) - B_0) f_A}{\sqrt{4\pi\rho(x)}}, \tag{10}$$

where $f_A$ is a free parameter (Zirakashvili & Ptuskin 2008; Lee et al. 2012). If scattering centers drift along the amplified field ($f_A = 1$), the Alfvénic drift will have the maximum effect. Here we will consider the models with $f_A = 0.5 - 1.0$ (see Table 1). For isotropic fields, the parallel magnetic field would be roughly $B_\parallel \approx B(x)/\sqrt{3}$. However, we simply use $B(x)$ for the Alfvén speed, since the uncertainties in this model is probably greater than a factor of $\sqrt{3}$.

In the postshock region the Alfvénic turbulence is probably relatively balanced, so the wave drift can be ignored, that is, $u_{w,2} \approx 0$ (Jones 1993). On the other hand, if the scattering centers drift away from the shock in both upstream and downstream regions, the accelerated particle spectrum could be softened drastically (e.g., Zirakashvili & Ptuskin 2008). We will consider one model (H2d) in which $u_{w,2} \approx -v_A$ is adopted in the downstream of the shock (see Table 1).

As mentioned in the Introduction, the CR spectrum develops a concave curvature when the preshock flow is modified by the CR pressure. If we include the Alfvénic drift only in the upstream flow, then the slope of the momentum distribution function, $q = -\partial \ln f/\partial \ln p$, can be estimated as

$$q_s \approx \frac{3(u_1 - u_{w,1})}{(u_1 - u_{w,1}) - u_2} \approx \frac{3\sigma_s(1 - M_{A,1}^{-1})}{\sigma_s(1 - M_{A,1}^{-1}) - 1} \tag{11}$$

for $p \sim p_{\rm inj}$, and

$$q_t \approx \frac{3(u_0 - u_{w,0})}{(u_0 - u_{w,0}) - u_2} \approx \frac{3\sigma_t(1 - M_{A,0}^{-1})}{\sigma_t(1 - M_{A,0}^{-1}) - 1} \tag{12}$$

for $p \sim p_{\rm max}$. Here $M_{A,1} = u_1/v_{A,1}$ is the Alfvénic Mach number immediately upstream of the subshock. As can be seen from these equations, significant steepening will occur only if $M_A \lesssim 10$ (Caprioli 2012).

According to the MFA prescription given in Eq. 7, the amplification factor depends on the precursor modification, that is, the ratio $B(x)/B_0$ is unity far upstream and increases through the precursor toward the subshock. So the Afvénic drift speed is highest immediately upstream of the subshock, while it is the same as the unperturbed Alfvén speed, $v_{A,0}$ at the far upstream region ($M_{A,1} \ll M_{A,0}$). Thus the Alfvénic drift is expected to steepen preferentially the lower energy end of the CR spectrum, since the lowest energy particles diffuse mostly near the subshock. For the highest energy particles, which diffuse over a distance of $\sim \kappa(p_{\rm p,max})/u_s$, however, the Alfévnic drift does not steepen the CR spectrum significantly, if $M_{A,0} \gg 1$.

**Table 1.** Model Parameters[a]

| Model[b] | $u_s$ km s$^{-1}$ | $n_H$ (ISM) (cm$^{-3}$) | $T_0$ (K) | $M_s$ | $M_{A,0}$ | $f_A$ [c] | $\omega_H$ [d] | $u_{w,1}$ | $u_{w,2}$ |
|---|---|---|---|---|---|---|---|---|---|
| W1a | $3\times10^3$ | 1.0 | $4.0\times10^4$ | 100 | 164. | 1.0 | 0.1 | $+v_A$ | 0 |
| W1b | $3\times10^3$ | 1.0 | $4.0\times10^4$ | 100 | 164. | 1.0 | 0.1 | 0 | 0 |
| H1a | $3\times10^3$ | 1.0 | $10^6$ | 20 | 164. | 1.0 | 0.1 | $+v_A$ | 0 |
| H1b | $3\times10^3$ | 1.0 | $10^6$ | 20 | 164. | 1.0 | 0.1 | 0 | 0 |
| H1c | $3\times10^3$ | 1.0 | $10^6$ | 20 | 164. | 0.5 | 0.5 | $+v_A$ | 0 |
| H2a | $3\times10^3$ | 0.01 | $10^6$ | 20 | 16.4 | 1.0 | 0.1 | $+v_A$ | 0 |
| H2b | $3\times10^3$ | 0.01 | $10^6$ | 20 | 16.4 | 1.0 | 0.1 | 0 | 0 |
| H2d | $3\times10^3$ | 0.01 | $10^6$ | 20 | 16.4 | 1.0 | 0.1 | $+v_A$ | $-v_A$ |
| H3a | $10^3$ | 0.01 | $10^6$ | 6.67 | 5.46 | 1.0 | 0.1 | $+v_A$ | 0 |
| H3b | $10^3$ | 0.01 | $10^6$ | 6.67 | 5.46 | 1.0 | 0.1 | 0 | 0 |
| H4a | $4.5\times10^3$ | 0.01 | $10^6$ | 30 | 24.6 | 1.0 | 0.1 | $+v_A$ | 0 |
| H4b | $4.5\times10^3$ | 0.01 | $10^6$ | 30 | 24.6 | 1.0 | 0.1 | 0 | 0 |

[a] For all the models the background magnetic field is $B_0 = 5\ \mu$G and the injection parameter is $\epsilon_B = 0.23$.
[b] 'W' and 'H' stand for the warm and hot phase of the ISM, respectively.
[c] See (9) for the Alfvén parameter.
[d] See Eq. 6 for the wave dissipation parameter.

### 2.6 Wave Dissipation and Particle Escape

As discussed in the Introduction, non-linear wave damping and dissipation due to ion-neutral collisions may weaken the stochastic scattering, leading to slower acceleration and escape of highest energy particles from the shock. These processes are not well understood quantitatively, so we adopt a simple model in which waves are dissipated locally as heat in the precursor. Then the gas heating term in the upstream region is prescribed as

$$W(x,t) = -\omega_H \cdot v_A(x)\frac{\partial P_c}{\partial x}, \tag{13}$$

where $P_c$ is the CR pressure (Jones 1993). The parameter $\omega_H$ is introduced to control the degree of wave dissipation and a fiducial value of $\omega_H = 0.1$ is assumed. As shown previously in SNR simulations (e.g., Berezhko & Völk 1997; Kang & Jones 2006), this precursor heating reduces the subshock Mach number thereby reducing the DSA efficiency. For larger values of $\omega_H$, the magnetic field amplification is suppressed (see Eq. 7), which also reduces the maximum momentum of protons and as a result the DSA efficiency.

In addition, we implement a free escape boundary (FEB) at an upstream location by setting $f(x_{\rm FEB}, p) = 0$ at $x_{\rm FEB} = 0.1R_s = 0.3$pc (here the shock is located at $x_s = 0$). This FEB condition can mimic the escape of the highest energy particles with the diffusion length, $\kappa(p)/u_s \gtrsim x_{\rm FEB}$. For typical supernova remnant shocks, this FEB leads to the size-limited maximum momentum,

$$\frac{p_{\rm p,max}}{m_p c} \approx 4.4\times10^4 (\frac{B_0}{5\mu{\rm G}})(\frac{u_s}{3000\ {\rm km\ s^{-1}}})(\frac{x_{\rm FEB}}{0.3{\rm pc}}). \tag{14}$$

As can be seen in Section 3, the CR proton spectrum and the shock structure approach the time-asymptotic states, if this FEB is employed (Kang et al. 2009).

The maximum electron momentum can be estimated by

$$\frac{p_{\rm e,max}}{m_p c} \approx 2.8\times10^4 \left(\frac{B_1}{30\ \mu{\rm G}}\right)^{-1/2} \left(\frac{u_s}{3000\ {\rm km\ s^{-1}}}\right), \tag{15}$$

which is derived from the equilibrium condition that the DSA momentum gains per cycle are equal to the synchrotron/IC losses per cycle (Kang 2011). The electron spectrum *at the shock position*, $f_e(x_s, p)$, cuts off exponentially at $\sim p_{\rm e,max}$.

On the other hand, the postshock electron spectrum cuts off at a progressively lower momentum downstream from the shock due to the energy losses. That results in the steepening of the volume integrated electron energy spectrum, $F_e(p) = \int f_e(x,p)dx$, by one power of the momentum (Kang et al. 2012). At the shock age $t$, the break momentum can be estimated from the condition $t = p/b(p)$:

$$\frac{p_{\rm e,br}(t)}{m_p c} \approx 1.3\times10^3 \left(\frac{t}{10^3\ {\rm yr}}\right)^{-1} \left(\frac{B_{\rm e,2}}{100\ \mu{\rm G}}\right)^{-2}, \tag{16}$$

which depends only on the postshock magnetic field strength and the shock age (Kang 2011).

### 2.7 Planar Shock Parameters

We consider planar shocks with $u_s = 1000 - 4500$ km s$^{-1}$, propagating into a uniform ISM magnetized with $B_0 = 5\ \mu$G. The model parameters are

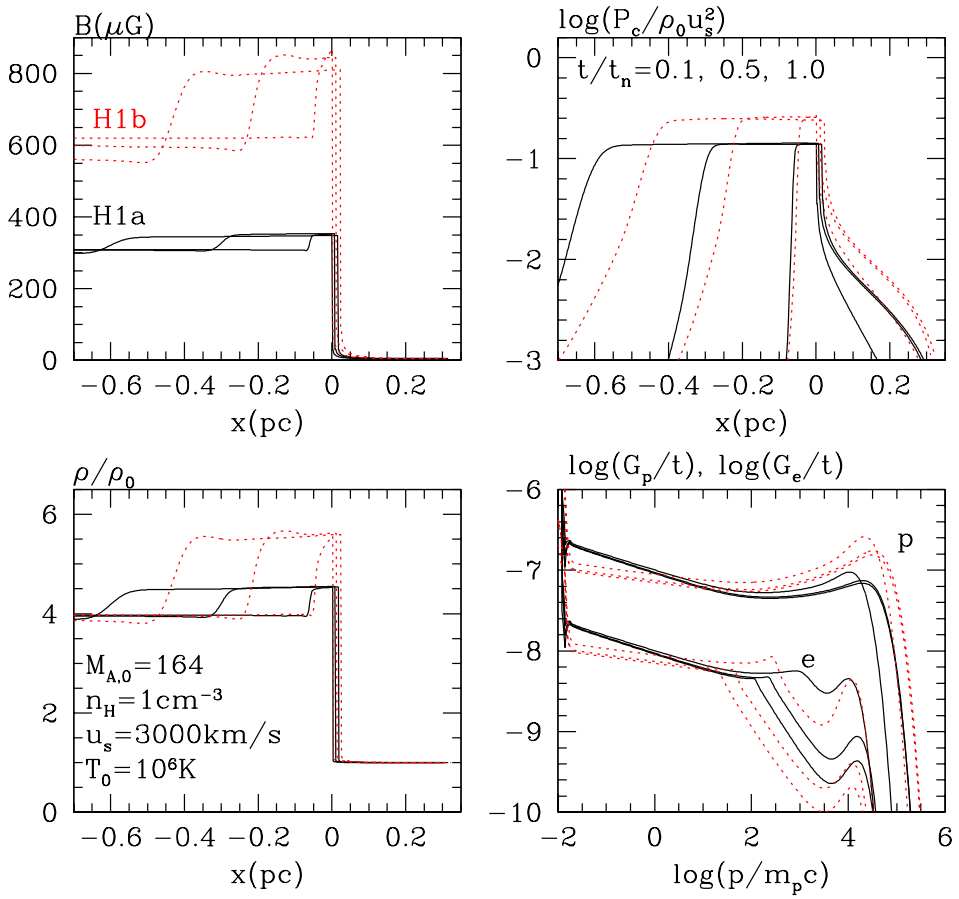


**Fig. 1.**— Time evolution of the magnetic field strength, CR pressure, gas density, and volume integrated distribution functions of protons ($G_p$) and electrons ($G_e$) for H1a (solid lines) and H1b (dotted lines) models at $t/t_n =$ 0.1, 2.5 and 5. See Table 1 for other model parameters and normalization constants. In the bottom right panel the upper curves are for the proton spectra, while the lower curves are for the electron spectra. Note that both $G_p/t$ and $G_e/t$ are given in arbitrary units and $K_{e/p} = 0.1$ is adopted here for clarity.

summarized in Table 1. Previous studies have shown that the shock sonic Mach number is one of the key parameter governing the evolution and the DSA efficiency (e.g., Kang & Jones 2007; Kang et al. 2009), and so two phases of the ISM are considered here: the *warm phase* with $T_0 = 4\times10^4$K (W models), and the *hot phase* with $T_0 = 10^6$K (H model). The sonic Mach number of each model is given as $M_s = 20(T_0/10^6\mathrm{K})^{-1/2}u_{3000}$, where $u_{3000} = u_s/3000$ km s$^{-1}$. Two values of the gas density $n_H = 0.01$ cm$^{-3}$ and 1 cm$^{-3}$ are considered. The upstream Alfvén speed is then $v_{A,0} = B_0/\sqrt{4\pi\rho_0} = (18.3\ \mathrm{km\ s^{-1}})n_H^{-1/2}$, so the Alfvénic Mach number is $M_{A,0} = u_s/v_{A,0} = 164\sqrt{n_H}u_{3000}$.

We consider W1a, H1a, H2a, H3a and H4a models as fiducial cases with canonical values of model parameters: $f_A = 1.0$ and $\omega_H = 0.1$. In models H1b, H2b, H3b and H4b, Alfvénic drift is turned off ($u_{w,1} = 0$) for comparison. But we note that these models are not self-consistent with our MFA model, which assumes that Alfv́en waves propagate along the amplified magnetic field. In H1c model, MFA is reduced by setting $f_A = 0.5$ and $\omega_H = 0.5$ . Model H2d is chosen to see the effects of Alfvénic drift in the postshock region.

The physical quantities are normalized in the numerical code and in the plots by the following characteristic values: $u_n = u_s$, $x_n = R_s = 3$ pc, $t_n = x_n/u_n = (978\ \mathrm{yr})u_{3000}$, $\kappa_n = u_n x_n$, $\rho_n = (2.34\times10^{-24}\mathrm{g\ cm^{-3}})\cdot n_H$, and $P_n = \rho_n u_n^2 = (2.11\times10^{-7}\mathrm{erg\ cm^{-3}})\cdot n_H u_{3000}^2$.

## 3. DSA SIMULATION RESULTS

Figs. 1-3 show the spatial profiles of the model magnetic field, CR pressure, gas density, and the volume integrated distribution functions of protons ($G_p = \int g_p(x,p)dx$) and electrons ($G_e = \int g_e(x,p)dx$) for H1a and H1b ($M_{A,0} = 164$), H2a and H2b ($M_{A,0} = 16.4$), and H3a and Hb ($M_{A,0} = 5.46$) models, respectively. In these simulations, the highest level of refinement is $l_{\mathrm{g,max}} = 8$ and the factor of each refinement is two, so the ratio of the finest grid spacing to the base grid spacing is $\Delta x_8/\Delta x_0 = 1/256$ (Kang et al. 2002). Since Figs. 1-3 show the flow structure on the base grid,

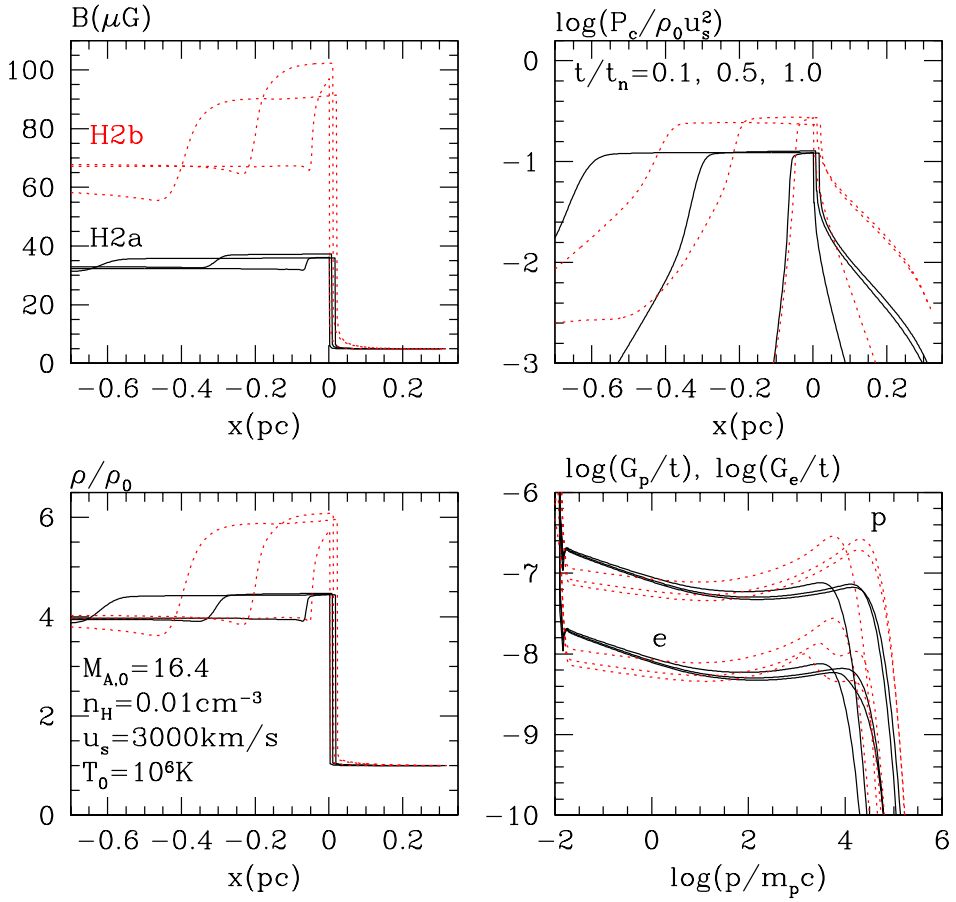


**Fig. 2.**— Same as Fig. 1 except that H2a (solid lines) and H2b (dotted lines) are shown.

the precursor profile may appear to be resolved rather poorly here. More accurate values of the precursor density compression ($\rho_1$) and magnetic field amplification ($B_1$) can be found in Fig. 4 below. Also note that the FEB is located at $x_{\rm FEB} = 0.3$pc and we use $K_{e/p} = 0.1$ here in order to show the proton and electron spectra together.

These figures demonstrate the following. 1) The shock structure reaches the time-asymptotic state and evolves in a self-similar fashion for $t/t_n \gtrsim 0.1$ (Kang & Jones 2007). 2) The proton spectrum approaches the steady state for $t/t_n \gtrsim 0.5$ due to the FEB, while the electron spectrum continues to cool down in the downstream region. 3) Magnetic field is amplified by a greater factor for a higher $M_{A,0}$. 4) Alfvénic drift steepens the CR spectrum, and reduces the CR acceleration efficiency and flow modification by CR feedback, resulting in lesser MFA. 5) At low energies the CR spectra are much steeper than the test-particle power-law due to the velocity profile and magnetic field structure in the precursor.

In H1a model with Alfvénic drift (solid lines), the gas density immediately upstream of the subshock increases to $\rho_1/\rho_0 \approx 1.2$, while the total compression ratio becomes $\rho_2/\rho_0 \approx 4.5$. So the flow structure is moderately modified by the CR pressure feedback: $U_1 \approx 0.9$ and $P_{c,2}/\rho_0 u_s^2 \approx 0.12$. Since the Alfvén Mach number is high ($M_{A,0} = 164$), the self-amplified magnetic field strength, based on the model in Eq. 7, increases to $B_1 \approx 100\mu$G, which results in the immediate postshock fields of $B_2 \approx 350\mu$G. Compared to the model without Alfvénic drift (H1b, dotted lines), the CR distribution functions are softer. Although Alfvénic drift steepens the distribution function in H1a model, $G_p(p)$ still exhibits a significant concave curvature and it is slightly flatter than the test-particle power-law ($E^{-2}$) at the highest energy end. This is because $M_{A,0} = 164$ is too large to induce significant enough softening for $p \sim p_{\rm p,max}$ (see Eq. 12). Note that $p_{\rm p,max}$ is lower in H1a model than that in H1b model, because of weaker MFA.

The structures of the integrated electron spectra are complex for $p \lesssim p_{\rm e,max}$. As shown in Eq. 16, the volume integrated electron energy spectrum steepens by one power of the momentum due to radiative cooling. One can see that the break momentum, $p_{\rm br}(t)$, shifts to lower momenta in time. The peak near $p_{\rm e,max}$ comes from the electron population in the upstream region, which cools much less efficiently due to weaker magnetic field there (Edmon et al. 2011). Since MFA is

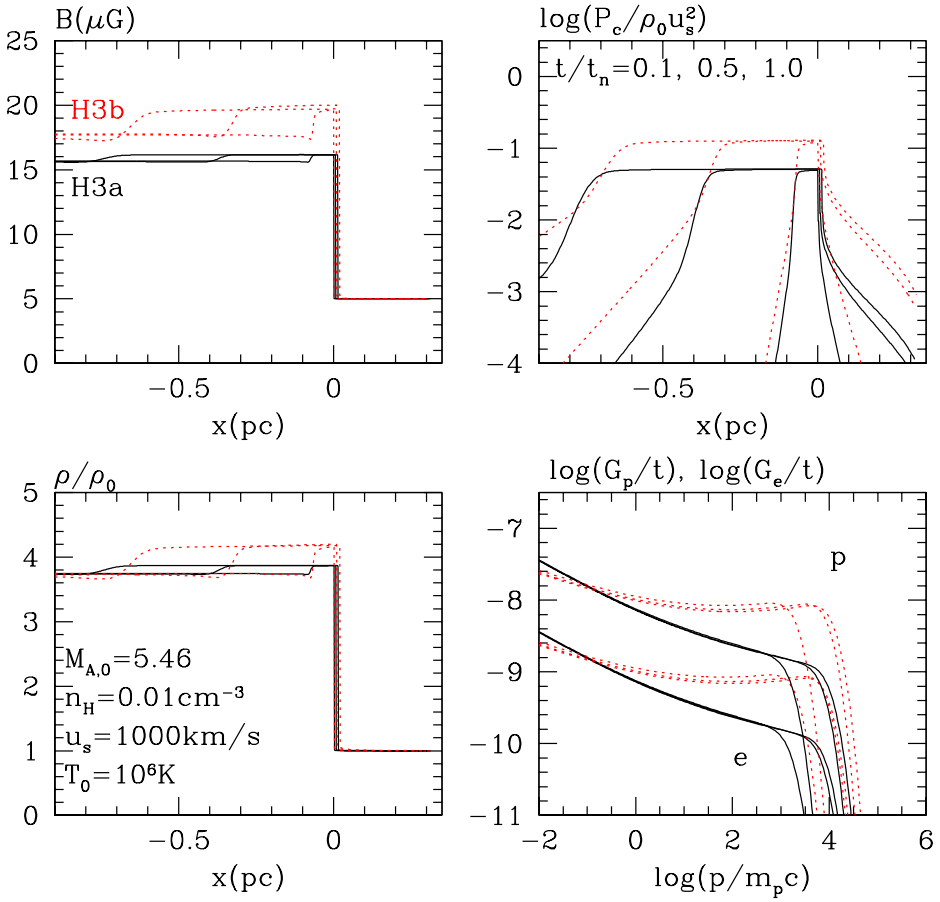


**Fig. 3.**— Same as Fig. 1 except that H3a (solid lines) and H3b (dotted lines) are shown.

much stronger in H1b model, compared to H1a model, the electron spectrum cools down to lower momentum in the downstream region.

Comparing H2a/b in Fig. 2 with H1a/b in Fig. 2, one can see that the degree of shock modification is similar in these models. Because of a lower gas density ($n_H = 0.01$ cm$^{-3}$) in H2a/b models, the Alfvén Mach number is smaller ($M_{A,0} = 16.4$) and so MFA is much less efficient, compared to H1a/b models. In H2a model the amplified preshock field increases to only $B_1 \approx 10$ $\mu$G, while the postshock field reaches $B_2 \approx 35$ $\mu$G. Because of much weaker magnetic field, compared to H1a/b model, the electron spectra are affected much less by radiative cooling.

Since H3a/b models in Fig. 3 have a lower sonic Mach Number ($M_s = 6.7$), the flow structures are almost test-particle like with $B_1 \approx B_0$, $\rho_2/\rho_0 \approx 4$, and $P_{c,2}/\rho_0 u_s^2 \approx 0.05 - 0.13$. So the CR acceleration, flow modification, and MFA are all less efficient, compared to H1a/b and H2a/b models. In H3a model, especially, the CR spectra are as steep as $E^{-2.1} - E^{-2.3}$ and electrons do not suffer significant cooling.

Fig. 4 shows how various shock properties change in time for different models: the CR injection fraction, postshock CR pressure, density compression factors and magnetic field strengths. As discussed above, the magnetic field amplification is more efficient in the models with higher $M_{A,0}$: $B_1/B_0 \approx 20$ for $M_{A,0} = 164$ (H1a, H1c, W1a models), $B_1/B_0 \approx 3$ for $M_{A,0} = 24.6$ (H4a), $B_1/B_0 \approx 2$ for $M_{A,0} = 16.4$ (H2a), $B_1/B_0 \approx 1$ for $M_{A,0} = 5.46$ (H3a).

According to previous studies, nonlinear DSA without self-consistent MFA and Alfvénic drift predicts that the DSA efficiency depends strongly on the sonic Mach number $M_s$ and the CR pressure asymptotes to $P_{c,2}/\rho_0 u_s^2 \sim 0.5$ for $M_s \gtrsim 20$ (Kang & Jones 2007; Kang et al. 2009). However, Fig. 4 shows that in the models with MFA and Alfvénic drift the CR acceleration and MFA are reduced in such a manner that the DSA efficiency saturates roughly at $P_{c,2}/\rho_0 u_s^2 \sim 0.1$ for $20 \lesssim M_s \lesssim 100$. We can see that models with a wide range of sonic Mach number, i.e., W1a ($M_s = 100$), H4a ($M_s = 30$), H2a and H1a ($M_s = 20$), all have similar results: $\rho_2/\rho_0 \approx 4.5$, and $P_{c,2}/\rho_0 u_s^2 \approx 0.1$.

Fig. 5 and 6 show the volume-integrated distribution function, $G_p(p)/(n_0 u_s t)$, for protons and, $G_e(p)/(n_0 u_s t)$, for electrons, respectively, for different models. Again the proton spectrum approaches the steady state for $t/t_n \gtrsim 0.5$, when $p_{\rm p,max}(t)$ satisfies the condition, $\kappa(p_{\rm p,max})/u_s \sim x_{\rm FEB}$. We note that

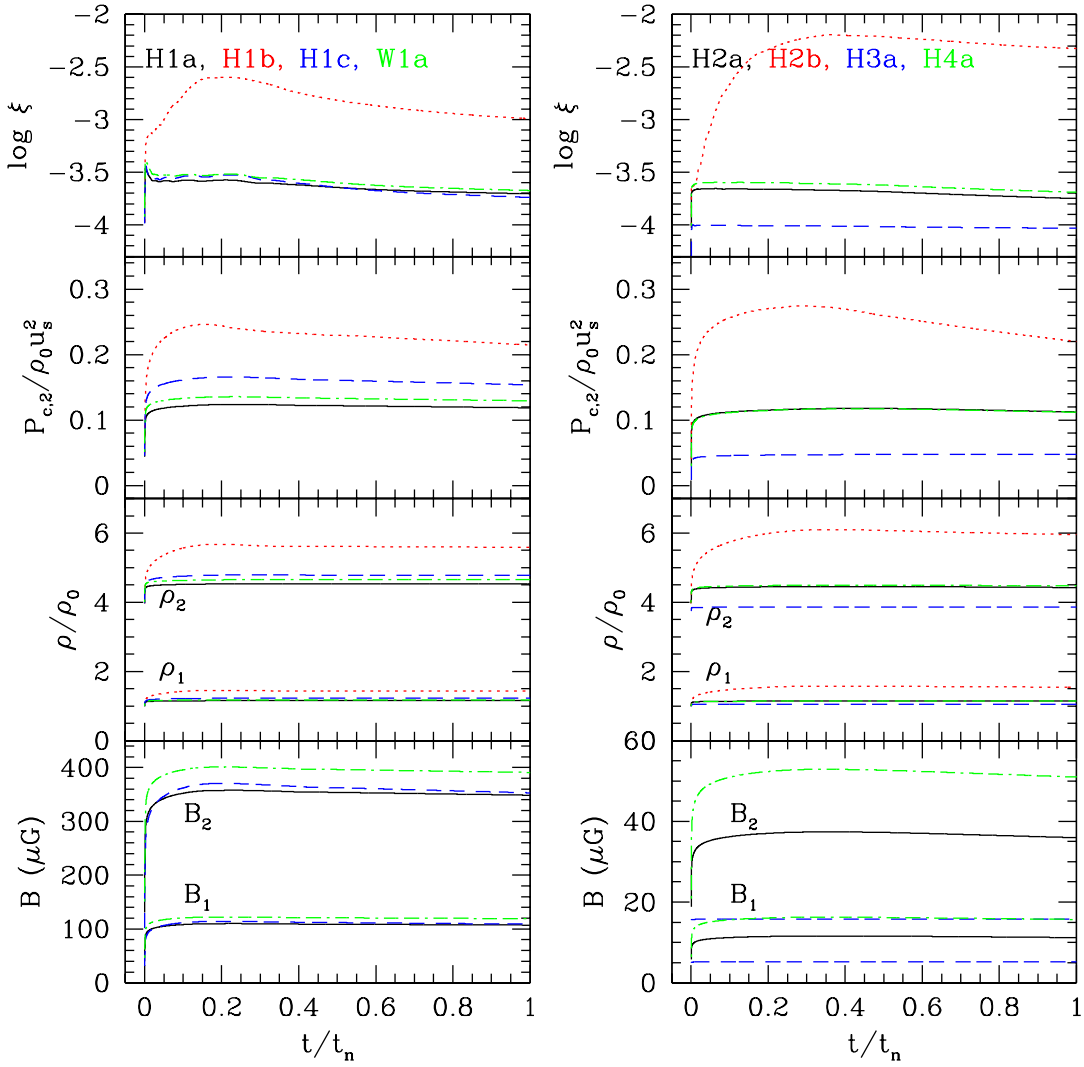


**Fig. 4.**— Time evolution of the injection efficiency, $\xi$, postshock CR pressure, $P_{c,2}$, the gas density $\rho_1$ ($\rho_2$) immediately upstream (downstream) of the subshock, and magnetic field strengths, $B_1$ and $B_2$, in different models: H1a (black solid lines), H1b (red dotted), H1c (blue dashed), W1a (green dot-dashed) in the left column, and H2a (black solid lines), H2b (red dotted), H3a (blue dashed), H4a (green dot-dashed) in the right column. Note H1b and H2b models are shown for comparison, but $B_1$ and $B_2$ for those models are not included in the bottom panels.

for W1b model only the curve at $t/t_n = 0.1$ is shown, because the simulation was terminated when the subshock disappears because of very efficient DSA. These figures demonstrate that the CR spectra is steepened by Alfvénic drift, especially at lower energies, and that the degree of softening is greater for smaller $M_{A,0}$. In H2d model, in which the downstream drift is included ($u_{w,2} = -v_A$) in addition to the upstream drift, the CR spectra are steepened drastically.

In the volume-integrated electron spectrum, the low-energy break corresponds to the momentum at which the electronic synchrotron/IC loss time equals the shock age. In the models with stronger magnetic field (e.g., H1a and W1a models), this spectral break occurs at a lower $p_{\rm e,br}$, and the separate peak around $p_{\rm e,max}$ composed of the upstream population becomes more prominent.

## 4. SUMMARY

Using the kinetic simulations of diffusive shock acceleration at planar shocks, we have calculated the time-dependent evolution of the CR proton and electron spectra for the shock parameters relevant for typical young supernova remnants. In order to explore how various wave-particle interactions affect the DSA process, we adopted the following phenomenological models: 1) magnetic field amplification (MFA) induced by CR streaming instability in the precursor, 2) drift of scattering centers with Alfvén speed in the amplified magnetic field, 3) particle injection at the subshock via thermal leakage injection, 4) Bohm-like diffusion coeffi-

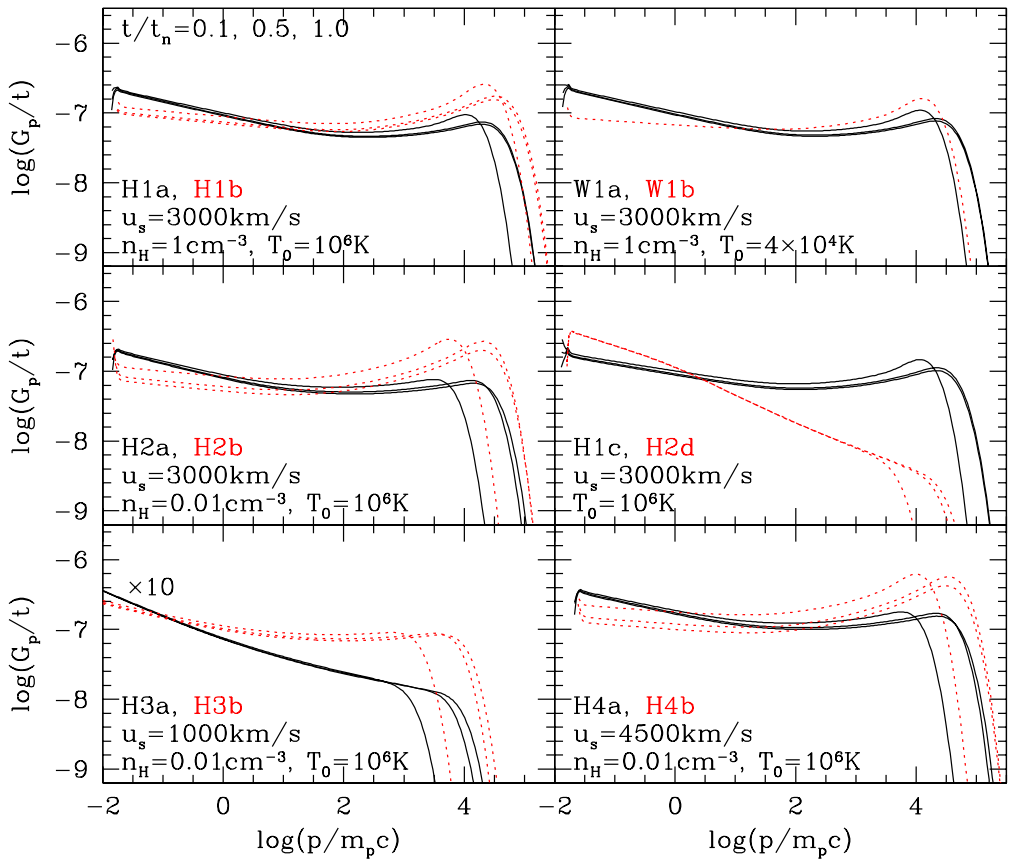


**Fig. 5.**— Volume integrated distribution function of CR protons for different models: H1a, W1a, H2a, H1c, H3a, H4a, (black solid lines), H1b, W1b, H2b, H2d, H3b, H4b (red dotted lines). For W1b model, only the curve for $t/t_n = 0.1$ is shown, because the simulation was terminated afterward. The curves for H3a/b are multiplied by a factor of 10 to show them in the same scale as other models. See Table 1 for model parameters.

cient, 5) wave dissipation and heating of the gas, and 6) escape of highest energy particles through a free escape boundary.

The MFA model assumes that the amplified magnetic field is isotropized by a variety of turbulent processes and so the Alfvén speed is determined by the *local amplified* magnetic field rather than the background field (Caprioli 2012). This model predicts that the magnetic field amplification factor scales with the upstream Alfvénic Mach number as $B_1/B_0 \propto M_{A,0}$, and also increases with the strength of the shock precursor (see Eq. 7).

Moreover, we assume that self-generated MHD waves drift away from the shock with respect to the background flow, leading to smaller velocity jumps that particles experience as they scatter across the shock. The ensuing CR distribution function becomes steeper than that calculated without Alfvénic drift. So the CR injection/acceleration efficiencies and the flow modification due to CR feed back are reduced.

The expected power-law slope depends on the Alfvénic Mach number as given in Eqs. 11-12. With our MFA model that depends on the precursor modification, the upstream Alfvénic drift affects lower energy particles more strongly, steepening the low energy end of the spectrum more than the high energy end. Hence, for $M_{A,0} \gtrsim 10$, the CR spectra still retain the concave curvature and they can be slightly flatter than $E^{-2}$ at the high energy end. For weaker shocks with $M_s = 6.7$ and $M_{A,0} = 5.5$ (H3a model), on the other hand, the Alfvénic drift effects are more substantial, so the energy spectrum becomes as steep as $N(E) \propto E^{-2.1} - E^{-2.3}$.

We can explain how MFA and Alfvénic drift regulate the DSA as follows. As CR particles stream upstream of the shock, magnetic field is amplified and Alfvén speed in the local $B(x)$ increases in the precursor. Then scattering centers drift with enhanced $v_A$, the CR spectrum is steepened and the CR acceleration efficiency is reduced, which in turn restrict the growth of the precursor (see also Caprioli 2012). So the flow modification due to the CR pressure is only moderate with $\rho_2/\rho_0 \approx 4.5$. As a result, the DSA efficiency saturates roughly at $P_{c,2}/\rho_0 u_s^2 \sim 0.1$ for $20 \lesssim M_s \lesssim 100$. For $M_s = 20$ shocks with $u_s = 3000$ km s$^{-1}$, for exam-

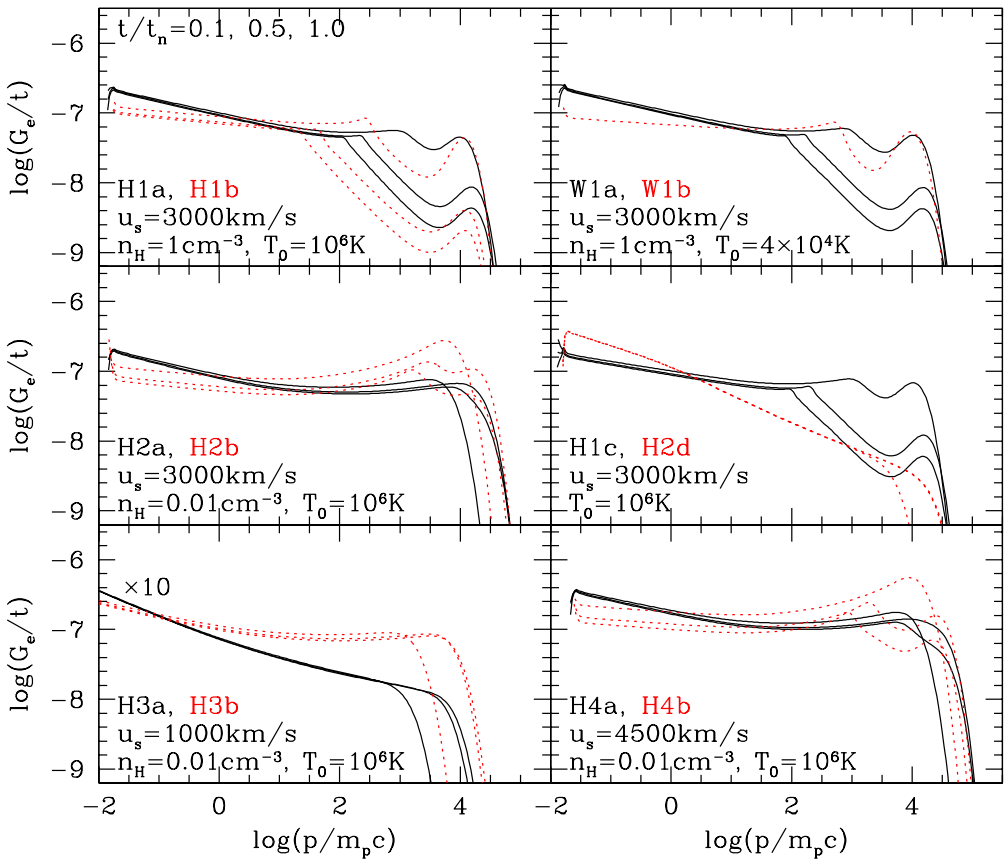


**Fig. 6.**— Same as Fig. 5 except that the volume integrated distribution function of CR electrons are shown.

ple, in the models with Alfvénic drift (H1a and H2a), the CR injection fraction is reduced from $\xi \sim 2 \times 10^{-3}$ to $\sim 2 \times 10^{-4}$, while the CR pressure decreases from $P_{c,2}/\rho_0 u_s^2 \sim 0.25$ to $\sim 0.12$, compared to the model without Alfvénic drift (H1b and H2b) (see Fig. 4).

This study demonstrates that detailed nonlinear treatments of wave-particle interactions govern the CR injection/acceleration efficiencies and the spectra of CR protons and electrons. Thus it is crucial to understand in a quantitative way how plasma interactions amplify magnetic fields and affect the transportation of waves in the shock precursor through detailed plasma simulations such as PIC and hybrid simulations. Moreover, the time-dependent behavior of self-amplified magnetic fields and CR injection as well as particle escape will determine the spectra of the highest energy particles accelerated at astrophysical shocks. We will present elsewhere the results from more comprehensive DSA simulations for a wide range of sonic and Alfvén Mach numbers.

## ACKNOWLEDGMENTS

This research was supported by Basic Science Research Program through the National Research Foundation of Korea (NRF) funded by the Ministry of Education, Science and Technology (2012-001065).

## REFERENCES

Abdo, A. A. et al. 2010, Fermi Large Area Telescope Observations of the Supernova Remnant W28 (G6.4-0.1), ApJ, 718, 348

Abdo, A. A. et al. 2011, Observations of the Young Supernova Remnant RX J1713.7-3946 with the Fermi Large Area Telescope, ApJ, 734,28

Acero, F. et al. 2010, First Detection of VHE $\gamma$-Rays from SN 1006 by HESS, A&A, 516, A62

Acciari, V. A., et al. 2011, Discovery of TeV Gamma-Ray Emission from Tycho's Supernova Remnant, ApJ, 730, L20

Ave, M., Boyle, P. J., Höppner, C., Marshall, J., & Müller, D. 2009, Propagation and Source Energy Spectral of Cosmic Ray Nuclei at High Energies, ApJ, 697, 106

Bell, A. R. 1978, The Acceleration of Cosmic Rays in Shock Fronts. I, MNRAS, 182, 147

Bell, A. R. 2004, Turbulent Amplification of Magnetic Field and Diffusive Shock Acceleration of Cosmic Rays, MNRAS, 353, 550

Berezhko, E. G., & Völk, H. J. 1997, Kinetic Theory of Cosmic Rays and Gamma Rays in Supernova Remnants. I. Uniform Interstellar Medium, Astropart. Phys., 7, 183

Berezhko, E. G., Ksenofontov, L. T., & Völk, H. J. 2009, Cosmic Ray Acceleration Parameters from Multi-Wavelength Observations. The Case of SN 1006, A&A, 505, 169

Blandford, R. D., & Eichler, D. 1987, Particle Acceleration at Astrophysical Shocks - a Theory of Cosmic-Ray Origin, Phys. Rept., 154, 1

Caprioli, D., Blasi, P., Amato, E., & Vietri, M. 2009, Dynamical Feedback of Self-generated Magnetic Fields in Cosmic Ray Modified Shock, MNRAS, 395, 895

Caprioli, D. 2012, Cosmic-Ray Acceleration in Supernova Remnants: Non-Linear Theory Revised, JCAP, 7, 38

Drury, L. O'C. 1983, An Introduction to the Theory of Diffusive Shock Acceleration of Energetic Particles in Tenuous Plasmas, Rept. Prog. Phys., 46, 973

Drury, L. O'C. 2011, Escaping the Accelerator: How, When and in What Numbers Do Cosmic Rays Get out of Supernova Remnants?, MNRAS, 415, 1807

Edmon, P. P., Kang, H., Jones, T. W., & Ma, R. 2011, Non-Thermal Radiation from Type Ia Supernova Remnants, MNRAS, 414, 3521

Eriksen, K. A., Hughes, J. P., Badenes, C., et al. 2011, Evidence for Particle Acceleration to the Knee of the Cosmic Ray Spectrum in Tycho's Supernova Remnant, ApJ, 728, L28

Garaté L., & Spitkovsky, A. 2012, Ion Acceleration in Non-relativistic Astrophysical Shocks, ApJ, 744, 67

Giordano, F., et al. 2012, Fermi Large Area Telescope Detection of the Young Supernova Remnant Tycho, ApJ, 744, L2

Guo, F., Jokipii, J. R., & Kota, J. 2010, Particle Acceleration by Collisionless Shocks Containing Large-Scale, Magnetic-Field Variations, ApJ, 725, 128

Jones, T. W. 1993, Alfvén Wave Transport Effects in the Time Evolution of Parallel Cosmic-Ray-Modified Shocks, ApJ, 413, 619

Kang, H. 2010, Cosmic Ray Spectrum in Supernova Remnant Shocks, JKAS, 43, 25

Kang, H. 2011, Energy Spectrum of Nonthermal Electrons Accelerated at a Plane Shock, JKAS, 44, 39

Kang, H., Edmon, P. P., & Jones, T. W. 2012, Non-Thermal Radiation from Type Ia Supernova Remnants, ApJ, 745, 146

Kang, H., & Jones, T. W. 2006, Numerical Studies of Diffusive Shock Acceleration at Spherical Shocks, Astropart. Phys., 25, 246

Kang, H., & Jones, T. W. 2007, Self-Similar Evolution of Cosmic-Ray-Modified Quasi-Parallel Plane Shocks, Astropart. Phys, 28, 232

Kang, H., Jones, T. W., & Gieseler, U. D. J. 2002, Numerical Studies of Cosmic-Ray Injection and Acceleration, ApJ, 579, 337

Kang, H., Ryu, D., & Jones, T. W. 2009, Self Similar Evolution of Cosmic-Ray Modified Shocks: The Cosmic-Ray Spectrum, ApJ, 695, 1273

Lee, S., Ellison, D. C., & Nagataki, S. 2012, A Generalized Model of Nonlinear Diffusive Shock Acceleration Coupled to an Evolving Supernova Remnant, ApJ, 750, 156

Lucek, S. G., & Bell, A. R. 2000, Non-Linear Amplification of a Magnetic Field Driven by Cosmic Ray Streaming, MNRAS, 314, 65

Malkov M. A., & Drury, L.O'C. 2001, Nonlinear Theory of Diffusive Acceleration of Particles by Shock Waves, Rep. Progr. Phys., 64, 429

Malkov M. A., Diamond, P. H., & Sagdeev, R. Z. 2011, Mechanism for Spectral Break in Cosmic Ray Proton Spectrum of Supernova Remnant W44, Nature Communications, 2, 194

Morlino G., & Caprioli, D. 2012, Strong Evidence for Hadron Acceleration in Tycho's Supernova Remnant, A&A, 538, 81

Parizot, E., Marcowith, A., Ballet, J., & Gallant, Y. A. 2006, Observational Constraints on Energetic Particle Diffusion in Young Supernovae Remnants: Amplified Magnetic Field and Maximum Energy, A&A, 453, 387

Ptuskin, V. S., & Zirakashvili, V. N. 2005, On the Spectrum of High-Energy Cosmic Rays Produced by Supernova Remnants in the Presence of Strong Cosmic-Ray Streaming Instability and Wave Dissipation, A&A, 429, 755

Ptuskin, V. S., Zirakashvili, V. N., & Seo, E. 2010, Spectrum of Galactic Cosmic Rays Accelerated in Supernova Remnants, ApJ, 718, 31

Reynolds, S. P. 2008, Supernova Remnants at High Energy, ARA&A, 46, 89

Reynolds, S. P., Gaensler, B. M., & Bocchino, F. 2012, Magnetic Fields in Supernova Remnants and Pulsar-Wind Nebulae, Space Sci. Rev., 166, 231

Riquelme, M. A., & Spitkovsky, A. 2009, Nonlinear Study of Bell's Cosmic Ray Current-Driven Instability, ApJ, 694, 626

Rogachevskii, I., Kleeorin, N., Brandenburg, A., & Eichler, D. 2012, Cosmic-Ray Current-Driven Turbulence and Mean-Field Dynamo Effect, ApJ, 753, 6

Skilling, J. 1975, Cosmic Ray Streaming. I - Effect of Alfvén Waves on Particles, MNRAS, 172, 557

Zirakashvili, V. N., & Ptuskin, V. S. 2008, Diffusive Shock Acceleration with Magnetic Amplification by Nonresonant Streaming Instability in Supernova Remnants, ApJ, 678, 939